

FAILURE-MODE TRANSITION SPEED IN THREE-DIMENSIONAL TRANSIENT DEFORMATIONS OF A MICROPOROUS HEAT-CONDUCTING THERMOELASTOVISCOPLASTIC PRENOTCHED PLATE

R. C. Batra and Zhicun Wang

Department of Engineering Science and Mechanics, Virginia Polytechnic Institute and State University, Blacksburg, Virginia, USA

We analyze three-dimensional finite coupled thermomechanical deformations of a rectangular plate with two parallel notches placed symmetrically about the horizontal centroidal plane of the plate. The edge surface of the plate between the two notches is struck by a cylindrical projectile of diameter equal to the distance between the notches and made of the same material as the plate. The plate material is modeled as heat-conducting, microporous, elastoviscoplastic, and isotropic. Both the brittle and the ductile failures initiate at points adjoining the notch-tip surface that are on the midplane of the plate and propagate toward the outer surfaces. Even for a relatively thin plate, the difference in the times of initiation of failures on the mid and front surfaces is significant. Also the two failure modes on the mid surface initiate much later than that predicted by the plane strain analysis. Thus an experimentalist observing fracture on the front or the back face of the plate will see it initiate much later than the times given by the plane strain analysis of the problem. For a steel plate, it is found that the failure mode transitions from brittle to ductile at an impact speed of about 21.8 m/s.

Keywords: Brittle and ductile failures; Coupled thermomechanical problem; Finite element solution; Impact load; Three-dimensional deformations

Kalthoff [1] summarized his experimental studies on transient deformations of a prenotched maraging steel plate with the axes of the two notches parallel to the top and the bottom edges of the plate; see Figure 1. The edge surface between the two notches is struck by a cylindrical projectile of diameter equal to the distance between the notches. With an increase in the impact speed, the failure mode transitioned from brittle failure in the form of a crack to ductile failure in the form of an adiabatic shear band (ASB). Numerical analyses of the problem are presented in refs. [2]–[10]. Of these nine works, eight [3–9] analyzed plane strain

Received 14 June 2004; accepted 6 December 2004.

This work was partially supported by the NSF (grant CMS0002849), the ONR (grants N00014-98-1-0300 and N00014-03-MP-2-0131), the ARO (grant DAAD19-01-1-0657), and the AFOSR MURI subcontract from Georgia Institute of Technology to Virginia Polytechnic Institute and State University. Opinions expressed in this article are those of the authors and not of the funding agencies.

Address correspondence to R. C. Batra, Department of Engineering Science and Mechanics, MC 0219, Virginia Polytechnic Institute and State University, Blacksburg, VA 24061, USA. E-mail: rbatra@vt.edu

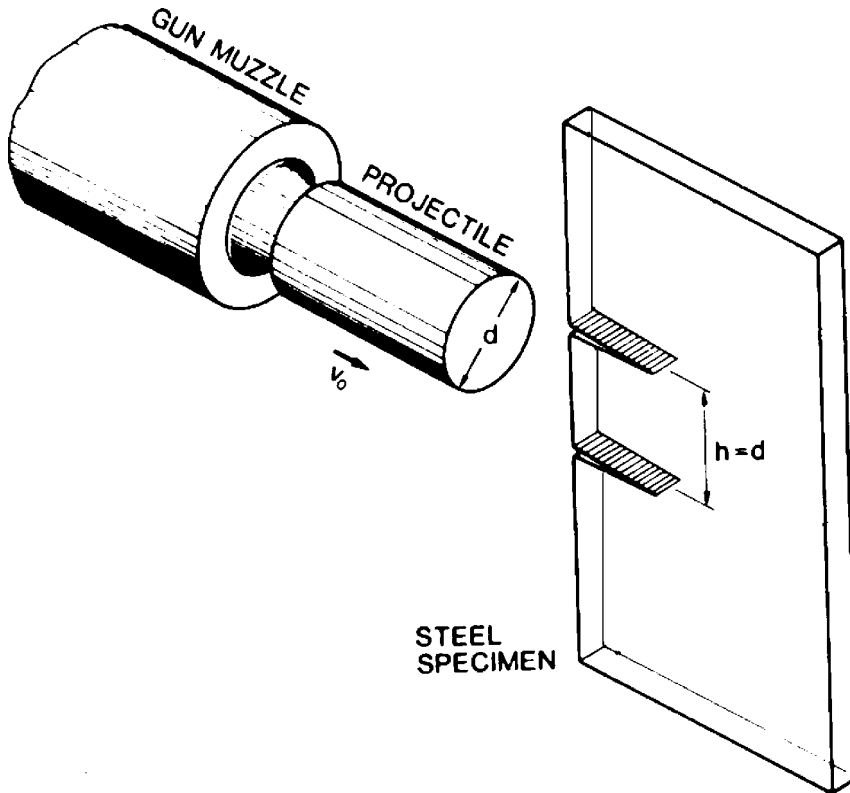


Figure 1 Schematic sketch of the problem studied.

deformations of the prenotched plate, and the one by Batra and Ravisankar [2] scrutinized three-dimensional (3-D) deformations of the plate and the projectile by using the finite-element (FE) computer code DYNA3D. The code neglects effects of heat conduction, thermal expansion, and porosity evolution on thermo-mechanical deformations of a body. Furthermore, it assumes stresses and temperature to be uniform within an eight-node brick element since it employs one-point integration rule. Also, Batra and Ravisankar [2] did not find the failure-mode transition speed. Batra and Jaber [7, 8] analyzed plane strain deformations and accounted for heat conduction, thermal expansion, and the porosity evolution. They assumed that a brittle failure initiates at a point when the maximum principal tensile stress there equals 2.34 times the quasistatic yield stress of the material, and the ductile failure in the form of an ASB initiates at a point when the effective stress there has dropped to 90% of the peak effective stress at that point while the material point is deforming plastically. They employed four constitutive relations, namely, the Johnson–Cook, the Batra–Litonski, the Bodner–Partom, and a power law. Each one of these was calibrated against the same test data by solving an initial-boundary-value problem closely resembling the experimental setup. Batra and Jaber [7] found that the four constitutive relations gave qualitatively similar deformations around the notchtip but predicted different failure mode

transition speeds. A similar result had been obtained earlier by Batra and Kim [11], who found that these four constitutive relations predicted different times of initiation of an ASB and also different postlocalization deformations. In a subsequent study, Batra et al. [9] analyzed the effect of the shape of the notch tip, and the presence of circular holes ahead of a circular notch tip. For an elliptic notch tip with the major axis aligned parallel to the notch axis, the brittle failure preceded the ductile failure for the six impact speeds studied, and for a blunt or a circular notch tip the failure mode transitioned from the brittle to the ductile with an increase in the impact speed. Batra et al. also examined the effect of the presence of a circular hole ahead of a circular notch tip and found that it shifted, toward the axis of the notch, the point on the notch-tip surface where an ASB initiated.

An experimental setup similar to that of ref. [1] has been employed by Mason et al. [12], Zhou et al. [13], and Ravi-Chandran et al. [14]. For the impact speeds and the notch-tip radius used in ref. [13], only a shear band initiated from a point on the notch surface, propagated into the plate, got arrested and then a crack initiated from the shear band tip. Zhou et al. [13] stated that the differences between their and Kalthoff's observations were due to the variation in material properties of the two steels tested. Ravi-Chandran et al. [14] examined experimentally failure modes in asymmetrically loaded prenotched plates made of two polymers, polycarbonate (PC) and polymethylmethacrylate (PMMA). With an increase in the impact speed, PC exhibited a transition from ductile to brittle failure at about 29 m/s, and a second transition from brittle to ductile failure as the impact speed was increased beyond 55 m/s. The second transition resulted in a shear band near the crack tip. No failure-mode transition occurred in PMMA because of its inability to undergo large inelastic tensile deformations.

Here we analyze 3-D thermomechanical deformations of the plate and account for the effects of heat conduction, thermal expansion, and porosity evolution on the failure-mode transition speed. Also, results from the 3-D solution are compared with those from the plane strain analysis of the problem. The present work differs from that of ref. [2] in the following respects. Here we consider heat conduction, porosity evolution due to the effective plastic strain exceeding a critical value, degradation of material parameters due to porosity evolution, and thermal stresses developed due to temperature gradients. Furthermore, stresses and the effective plastic strain at nodes are taken as unknowns in the numerical solution of the problem. We also compute the failure-mode transition speed, which was not determined in ref. [2]. An additional result is the propagation in the thickness direction of the brittle failure originating from a point slightly away from the notch surface but on the mid surface of the plate.

The article is organized as follows. The next section gives the problem formulation, and the third section the semidiscrete formulation. The computational technique is briefly described in the fourth section, which also lists the failure criteria and gives results for two FE meshes. Effects of porosity evolution and thermal stresses are delineated in the fourth and sixth subsection, respectively, and the failure-mode transition speed is listed in the fifth subsection. The seventh subsection compares results from the 3-D and the plane strain (2-D) simulations. Conclusions are summarized in the final section.

FORMULATION OF THE PROBLEM

A schematic sketch of the problem studied is shown in Figure 1. We neglect the effect of body forces and sources, if any, of the internal energy and employ the Lagrangian or the referential description of motion to describe deformations of the body. In the absence of body forces and sources of internal energy, thermomechanical deformations of the prenotched plate and the cylindrical projectile are governed by the following balance of mass (1), the balance of linear momentum (2), the balance of moment of momentum (3), and the balance of internal energy (4).

$$[\rho(1-f)J]' = 0 \quad (1)$$

$$\rho_0(1-f_0)\dot{\mathbf{v}} = \text{Div } \mathbf{T} \quad (2)$$

$$\mathbf{T}\mathbf{F} = \mathbf{F}^T\mathbf{T}^T \quad (3)$$

$$\rho_0(1-f_0)\dot{e} = -\text{Div } \mathbf{Q} + \text{tr}(\mathbf{T}\dot{\mathbf{F}}^T) \quad (4)$$

Here ρ is the present mass density, f the porosity (i.e., the volume fraction of voids), $J = \det \mathbf{F}$, $\mathbf{F} = \text{Grad } \mathbf{x}$ (the deformation gradient), \mathbf{x} the present position at time t of a material particle located at the place \mathbf{X} in the reference configuration, Grad (grad) the gradient operator with respect to coordinates in the reference (present) configuration, Div the divergence operator, tr the trace operator, \mathbf{T} the first Piola–Kirchhoff stress tensor, e the specific internal energy, \mathbf{Q} the present heat flux measured per unit reference area, \mathbf{v} the velocity of a material particle, and a superimposed dot indicates the material time derivative. Some of the equations that follow are written with respect to rectangular Cartesian coordinate axes; in these equations a repeated index implies summation over the range of the index.

We assume that the material is isotropic, the plate is homogeneous, and the strain-rate tensor \mathbf{D} defined by $2\mathbf{D} = \text{grad } \mathbf{v} + (\text{grad } \mathbf{v})^T$ has the additive decomposition into an elastic part \mathbf{D}^e and a plastic part \mathbf{D}^p , viz.,

$$\mathbf{D} = \mathbf{D}^e + \mathbf{D}^p \quad (5)$$

Equations (1)–(5) are supplemented with the following constitutive relations:

$$\dot{\sigma}_{ij} + \sigma_{ik}W_{kj} - \sigma_{jk}W_{ik} = \frac{E(1-f)}{1+\nu}D_{ij}^e + \frac{E(1-f)\nu}{(1+\nu)(1-2\nu)}(D_{kk}^e - \alpha\dot{\theta})\delta_{ij} \quad (6)$$

$$\dot{e} = c\dot{\theta} + \frac{1}{\rho(1-f)}\sigma_{ij}D_{ij}^e \quad (7)$$

$$T_{i\alpha} = J\sigma_{ij}(F^{-1})_{\alpha j} \quad (8)$$

$$q_i = -\kappa \left(1 - \frac{3}{2}f\right) \theta_{,i}, \quad Q_\alpha = Jq_i (F^{-1})_{\alpha i} \quad (9)$$

$$\phi \equiv \frac{\sigma_e^2}{\sigma_y^2} - 1 + 2f^* \beta_1 \cosh\left(\frac{3\beta_2 \bar{p}}{2\sigma_y}\right) - \beta_1^2 (f^*)^2 = 0, \quad \sigma_e^2 = \frac{3}{2} \sigma'_{ij} \sigma'_{ij}, \quad i, j = 1, 2, 3 \quad (10)$$

$$D_{ij}^p = \dot{\lambda} \frac{\partial \phi}{\partial \sigma_{ij}} = \dot{\lambda} \left[\frac{3\sigma'_{ij}}{\sigma_y^2} - \frac{f^* \beta_1 \beta_2}{\sigma_y} \sinh\left(\frac{\beta_2 \bar{p}}{2\sigma_y}\right) \delta_{ij} \right], \quad \sigma'_{ij} = \sigma_{ij} + p \delta_{ij} \quad (11)$$

$$p = -(\sigma_{11} + \sigma_{22} + \sigma_{33})/3, \quad \bar{p} = pH(-p - 0) \quad (12)$$

$$\dot{\lambda} = \begin{cases} \frac{(1-f)\sigma_y \dot{\epsilon}_e^p}{\sigma_{ij} \frac{\partial \phi}{\partial \sigma_{ij}}} & \text{if } \phi = 0 \text{ and } \dot{\phi} \geq 0 \\ 0 & \text{when either } \phi < 0 \text{ or } \phi = 0 \text{ and } \dot{\phi} < 0 \end{cases} \quad (13)$$

$$\dot{f} = (1-f)D_{ii}^p + \frac{f_2 \dot{\epsilon}_e^p}{s_2 \sqrt{2\pi}} e^{-\frac{1}{2} \left(\frac{\epsilon_e^p - \epsilon_n}{s_2}\right)^2} H(-p - 0) \quad (14)$$

$$f^* = \begin{cases} f, & f \leq f_c \\ f_c + \frac{f_u - f_c}{f_t - f_c} (f - f_c), & f > f_c \end{cases} \quad (15)$$

$$\sigma_y = [A + B(\epsilon_e^p)^n] \left[1 + C \ln\left(\frac{\dot{\epsilon}_e^p}{\dot{\epsilon}_0^p}\right)\right] \left[1 - \left(\frac{\theta - \theta_r}{\theta_m - \theta_r}\right)^m\right] \quad (16)$$

The left-hand side of Eq. (6) equals the Jaumann derivative of the Cauchy stress tensor $\boldsymbol{\sigma}$, $W_{ij} = (v_{i,j} - v_{j,i})/2$ is the spin tensor, E Young's modulus, ν Poisson's ratio, α the coefficient of thermal expansion, δ_{ij} the Kronecker delta, c the specific heat, τ the thermal relaxation time, κ the thermal conductivity of the solid material, and θ the present temperature of a material particle. Batra and Jaber [7] found that the Jaumann and the Green–Naghdi stress rates in Eq. (6) give virtually identical results for a shear band originating from a notch tip in a pre-notched plate. $\phi = 0$ describes the yield surface proposed by Gurson [15] for a porous material, p is the hydrostatic pressure, and f^* the modified value of the porosity given by Eq. (15). Constants β_1 and β_2 , introduced by Tvergaard [16], provide a better fit of results computed from a FE analysis of the formation of ASBs in a plate having an array of large cylindrical voids with test observations, and $\dot{\lambda}$ is the factor of proportionality defined by Eq. (13); $\dot{\lambda} > 0$ only when the material point is deforming plastically. σ_y is the current yield stress of the material, whose dependence upon the effective plastic strain ϵ_e^p , the effective

plastic strain rate $\dot{\epsilon}_e^p$, and the temperature θ is described by the Johnson–Cook [17] relation through Eq. (16) in which A , B , C , $\dot{\epsilon}_0^p$, and m are material parameters, θ_r the room temperature and θ_m the melting temperature of the material. Parameters B and n characterize the strain hardening of the material, C and $\dot{\epsilon}_0^p$ the strain-rate hardening, and the last factor on the right-hand side of Eq. (16) its thermal softening. Equation (14) gives the evolution of the porosity; the first term on its right-hand side is derived by assuming that the matrix is incompressible and the elastic dilatation is negligible as compared to the plastic dilatation, and the second term is the strain-based nucleation of voids introduced by Chu and Needleman [18]. Constants f_2 , s_2 , and ϵ_n are material parameters; the rate of nucleation of voids is highest when ϵ_e^p equals ϵ_n and decays exponentially with the difference between ϵ_e^p and ϵ_n . H is the Heaviside step function. Thus the second term contributes to the evolution of the porosity at a point only when the hydrostatic pressure there is tensile. To account for the coalescence of neighboring voids, Tvergaard and Needleman [19] enhanced the porosity, as given by Eq. (15), after it reaches its critical value f_c . In Eq. (15), f_f is the porosity at ductile fracture, and $f_u = 1/\beta_1$ is the porosity when the yield surface has shrunk to a point. Equations (10) and (16) imply that the radius of the von Mises yield surface increases due to strain- and strain-rate hardening of the material but decreases due to the softening induced by the temperature rise and the increase in porosity. The degradation of material properties due to the damage, taken here synonymous with the porosity, is indicated by Eq. (6) through (10). The affine variation with the porosity of Young's and the bulk moduli implies that the rule of mixture has been employed to find the effective moduli. The interaction, if any, among neighboring voids has been tacitly ignored. The shrinkage of the yield surface due to an increase in porosity described by Eq. (10) can be appreciated by plotting the yield surface for two different values of f while keeping other variables fixed. Perzyna [20] has given a different equation for the evolution of porosity.

Initial and boundary conditions needed to complete the formulation of the problem are:

$$\begin{aligned} \mathbf{x}(\mathbf{X}, 0) &= \mathbf{X}, \quad \mathbf{v}(\mathbf{x}, 0) = \mathbf{0}, \quad \theta(\mathbf{X}, 0) = \theta_r, \quad \rho(\mathbf{X}, 0) = \rho_0, \\ \epsilon_e^p(\mathbf{X}, 0) &= 0, \quad f(\mathbf{X}, 0) = f_0(\mathbf{X}) \\ \mathbf{T}\mathbf{N} &= \mathbf{0} \text{ on } \Gamma_t, \quad \mathbf{x} = \bar{\mathbf{x}} \text{ on } \Gamma_v, \quad \mathbf{Q} \cdot \mathbf{N} = 0 \text{ on } \partial\Omega \end{aligned} \quad (17)$$

That is, the plate is initially at rest, the initial temperature is uniform θ_r , and the initial mass density is uniform ρ_0 . Here \mathbf{N} is an outward unit normal to the surface $\partial\Omega$, and $\mathbf{A} \cdot \mathbf{B}$ denotes the inner product between vectors \mathbf{A} and \mathbf{B} . The part Γ_t of the boundary $\partial\Omega$ of the region Ω occupied by the body in the reference configuration is traction free and positions of material particles on Γ_v are given as a function of time. Γ_t and Γ_v have been taken to be disjoint for simplicity. Boundary conditions involving the prescription of linearly independent components of $\mathbf{T}\mathbf{N}$ and \mathbf{x} at the same point on $\partial\Omega$ are admissible. The entire boundary $\partial\Omega$ is thermally insulated at all times; it is reasonable to assume so since time durations of interest are of the order of 100 μs and there is not much heat transferred through the boundaries under ordinary conditions.

Substitution from Eqs. (5), (7), and (9) into (4) gives the following parabolic heat equation:

$$\rho_0(1-f_0)c\dot{\theta} = \text{Div} \left(\kappa \left(1 - \frac{3}{2}f \right) \text{Grad } \theta \right) + J \text{tr}(\boldsymbol{\sigma}\mathbf{D}^P) \quad (18)$$

The term $\text{tr}(\boldsymbol{\sigma}\mathbf{D}^P)$ equals the heating due to plastic working; thus the Taylor–Quinney parameter has been set equal to 1. Except for a delay in the time of initiation of an ASB, other results remain unaffected by a lower value of the Taylor–Quinney factor.

Let ρ_0 , $\dot{\epsilon}_R$, L_c , σ_0 , and θ_R be the reference mass density, the reference strain rate ($=V_0/L_c$), the reference length, the reference stress, and the reference temperature used to nondimensionalize quantities. Then in terms of nondimensional variables indicated by the same symbols as before, Eqs. (2) and (18) become

$$\alpha_I(1-f_0)\dot{\mathbf{v}} = \text{Div } \mathbf{T}, \quad (19)$$

$$(1-f_0)\dot{\theta} = -\alpha_t \text{Div} \left[\left(1 - \frac{3}{2}f \right) \text{Grad } \theta \right] + J \text{tr}(\boldsymbol{\sigma}\mathbf{D}^P) \quad (20)$$

where

$$\alpha_I = \frac{\rho_0 \dot{\epsilon}_R^2 L_c^2}{\sigma_0}, \quad \alpha_t = \frac{\kappa}{\rho_0 c L_c^2 \dot{\epsilon}_R}, \quad \theta_R = \frac{\sigma_0}{\rho_0 c} \quad (21)$$

and α_I and α_t are nondimensional measures of inertia and heat conduction. Thus, for a given material, inertia effects are directly proportional to the square of the reference strain rate and the square of the reference length, and heat conduction effects are inversely proportional to the reference strain rate and the square of the reference length.

In order to reduce the problem size, we do not analyze deformations of the projectile and replace its action on the prenotched plate by prescribing the normal component of velocity on the smooth impacted surface of the plate. The normal velocity is taken to increase linearly with time from 0 to $0.9V_0$ in $5\mu\text{s}$ and then stay steady at $0.9V_0$; V_0 is the speed of the projectile. It approximates the average normal velocity of plate particles on the impacted surface computed by Batra and Ravisankar [2] from their 3-D analysis of deformations of the projectile and the plate. The time is reckoned from the instant of impact. As noted by Ravi-Chandar et al. [14], a one-dimensional analysis of impact between two bodies having unequal areas at the contact surface reveals that the normalized axial velocity imparted to a plate particle equals $(1 + A_p/A_r)^{-1} = 0.861$. Here A_p and A_r are, respectively, the impacted area of the plate and the area of cross section of the projectile. Thus the one-dimensional (1-D) analysis gives a good approximation of the maximum speed of plate particles on the impacted face but provides no information of the rise time.

For a 100-mm-long steel projectile striking at normal incidence the edge of a 100-mm-wide steel plate, the two will separate at $t \simeq 34\mu\text{s}$. Since results have been

computed for $t < 34 \mu\text{s}$, the separation between the projectile and the plate has not been considered. After separation, the impacted face of the plate will be traction free. Thus boundary conditions on it will need to be modified; e.g., see ref. [10].

SEMIDISCRETE FORMULATION OF THE PROBLEM

Equations (5), (6), (8), and (3) imply that the balance of moment of momentum expressed by Eq. (3) is identically satisfied. The present mass density can be computed from Eq. (1) if the deformation gradient and the current value of the porosity are known. Thus, the dependent variables to be solved for are \mathbf{x} , f , and θ and the independent variables are \mathbf{X} and t . Equation (19) is a set of three second-order coupled nonlinear hyperbolic partial differential equations for \mathbf{x} , and Eq. (20) is a nonlinear parabolic partial differential equation for θ . These can not be written explicitly in terms of \mathbf{x} and θ since \mathbf{T} is given by Eq. (8) and $\dot{\boldsymbol{\sigma}}$ by Eq. (6), which involves \mathbf{D}^p and θ . We solve the problem numerically by the finite-element method (FEM).

Let $\psi_1, \psi_2, \dots, \psi_n$ be the FE basis functions defined on Ω . We write

$$v_i = \sum_{A=1}^{\text{nodes}} \psi_A(\mathbf{X}) \tilde{v}_{Ai}(t), \quad w_i = \sum_{A=1}^{\text{nodes}} \psi_A(\mathbf{X}) c_{Ai}, \quad \theta = \psi_A(\mathbf{X}) \tilde{\theta}_A(t), \quad i = 1, 2, 3 \quad (22)$$

Here $\tilde{\mathbf{v}}$ is the vector of velocities of nodes, $\tilde{\boldsymbol{\theta}}$ the vector of nodal temperatures, \mathbf{w} the vector of virtual velocities or test functions, and \mathbf{c} the vector of arbitrary constants. Taking the inner product of both sides of Eq. (19) with \mathbf{w} , integrating both sides of the resulting equation over the domain Ω occupied by the body in the reference configuration, using the divergence theorem on the right-hand side, requiring that \mathbf{w} vanish wherever \mathbf{v} or \mathbf{x} is prescribed, substituting for $\mathbf{T}\mathbf{N}$ from Eq. (17)₇, and noting that the final equation thus obtained must hold for all choices of \mathbf{c} , we get Eq. (23)₁. A similar procedure applied to Eq. (20) gives Eq. (23)₂; for example, see ref. [22].

$$\mathbf{M}\dot{\tilde{\mathbf{v}}} = -\mathbf{F}^{\text{int}}, \quad \mathbf{H}\dot{\tilde{\boldsymbol{\theta}}} = \mathbf{F}^\theta + \tilde{\mathbf{Q}} \quad (23)$$

where

$$\begin{aligned} M_{AB} &= \int_{\Omega} \alpha_I (1 - f_0) \psi_A \psi_B \, d\Omega, & F_{Ai}^{\text{int}} &= \int_{\Omega} \psi_{A,\alpha} T_{i\alpha} \, d\Omega \\ H_{AB} &= \int_{\Omega} (1 - f_0) \psi_A \psi_B \, d\Omega, & F_A^\theta &= \int_{\Omega} \alpha_i \left(1 - \frac{3}{2}f\right) \theta_{,\alpha} \psi_{A,\alpha} \, d\Omega \\ \tilde{Q}_A &= \int_{\Omega} \psi_A J \, \text{tr}(\boldsymbol{\sigma}\mathbf{D}^p) \, d\Omega \end{aligned} \quad (24)$$

Note that the natural boundary condition of zero heat flux has been embedded in Eq. (24)₅.

We solve Eq. (16) for $\dot{\epsilon}_e^p$ in terms of σ_y , ϵ_e^p , and θ and derive its weak form in the same way as before except that the divergence theorem is not used. Recall that $\dot{\epsilon}_e^p > 0$ only when a material point is deforming plastically as signified by the satisfaction of Eq. (10)₁; otherwise, $\dot{\epsilon}_e^p = 0$. Weak forms of Eqs. (6), (14), and $\dot{\mathbf{x}} = \mathbf{v}(\mathbf{X}, t)$ are

also derived. We thus get coupled nonlinear ordinary differential equations

$$\dot{\mathbf{d}} = \mathbf{F} \quad (25)$$

where \mathbf{d} is the vector of unknowns and \mathbf{F} is the force vector that depends upon time t and $\mathbf{d}(t)$. The 15 unknowns at a node are $\{x_1, x_2, x_3, v_1, v_2, v_3, \sigma_{11}, \sigma_{22}, \sigma_{33}, \sigma_{12}, \sigma_{23}, \sigma_{31}, f, \theta, \varepsilon_c^p\}$, and the dimension of vector \mathbf{d} equals 15 times the number of nodes.

COMPUTATION AND DISCUSSION OF RESULTS

The FE mesh is comprised of nonuniform eight-node brick elements. Note that the aforementioned Galerkin approximation of the problem incorporates the natural boundary conditions of surface tractions and the heat flux and results in a system of coupled ordinary differential equations (ODEs) for the nodal positions, the nodal velocities, the nodal temperatures, the nodal stresses, the nodal porosities, and the nodal effective plastic strain rates. The mass of each element remains unchanged during the deformation process; thus the mass matrix needs to be computed only once. The domain integrals are evaluated by using the $2 \times 2 \times 2$ Gauss quadrature rule. Boundary conditions on velocity are enforced by modifying the mass matrix and the force vector. The ODEs are integrated with respect to time t by using the subroutine LSODE that adaptively adjusts the time-step size to compute the solution within the prescribed tolerance. Our approach is similar to that of Batra and Jin [21], with the difference that we use total Lagrangian description of motion and they employed the updated Lagrangian.

Because of the symmetry of the problem about the horizontal and the vertical centroidal planes, deformations of one-quarter of the plate are analyzed.

When computing results we assigned following values to various material and geometric parameters: $\rho_0 = 7,850 \text{ kg/m}^3$, $E = 196 \text{ GPa}$, $\nu = 0.29$, $A = 792.2 \text{ MPa}$, $\dot{\varepsilon}_0 = 1/\text{s}$, $B = 0.643A$, $n = 0.26$, $m = 1.03$, $C = 0.014$, $\theta_m = 760^\circ\text{C}$, $\theta_r = 25^\circ\text{C}$, $h = d = 50 \text{ mm}$ reference length = 100 mm, plate thickness = 6.35 mm, notch-tip radius = 0.15 mm, plate dimensions = 100 mm \times 200 mm, $V_0 = 50 \text{ m/s}$, $\beta_1 = 1.5$, $\beta_2 = 1.0$, $f_2 = 0.04$, $s_2 = 0.1$, $\sigma_0 = A$, $\varepsilon_n = 0.5$, $f_c = 0.15$, $f_u = 2/3$, $f_r = 0.25$.

These values are for 4340 steel, with the exception of the melting temperature, which is taken to be low so that an ASB will initiate sooner and computations will take less CPU time.

Computed results can not be compared with those of Kalthoff [1], since he only listed the Rockwell hardness number of the steel plate.

Code Validation

The validity of the code was established by solving the problem analyzed earlier by Batra and Ravisankar [2] with DYN3D. The same FE mesh with half of the plate thickness divided into 10 layers of equal thicknesses was employed. Results computed from the present code by neglecting effects of heat conduction, thermal expansion, and porosity evolution matched very well with those of ref. [2]. For

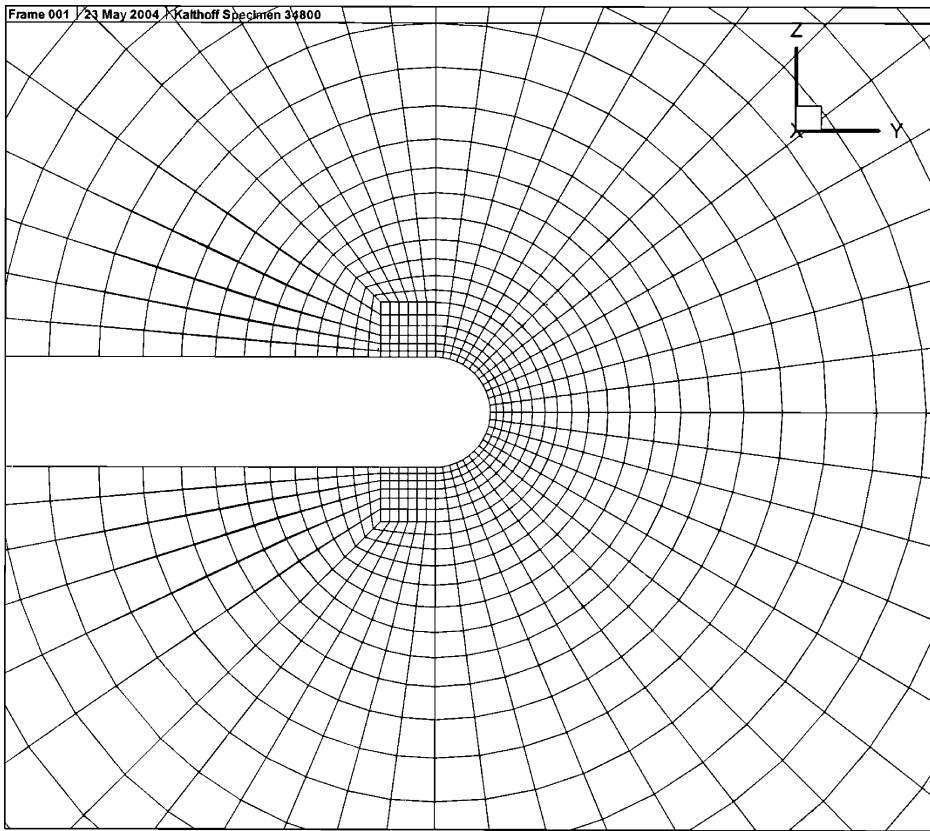


Figure 2 Discretization into finite elements of the region near the notch tip in the X_2X_3 plane.

identical FE meshes, DYNA3D predicted that an ASB will initiate at $t = 24 \mu\text{s}$, and our code gave $t = 23.84 \mu\text{s}$; the ASB initiation criterion is given in the next subsection. However, no brittle failure ensued when the problem was analyzed with DYNA3D, but it initiated at $29.68 \mu\text{s}$ according to the present code.

The average speeds of propagation of an ASB in the axial (plate-thickness) direction according to results from DYNA3D and the present code equal 440 m/s and 372 m/s , respectively. As shown in Figure 8 of ref. [2], the ASB speed according to results from the present code decreased as it propagated axially from the midsurface to the front face from 1984 m/s to 104 m/s . Also in agreement with the results from DYNA3D, the angular position of the point of initiation of the ASB in surfaces 1 (midsurface) through 9 remained the same but it was different on surfaces 10 and 11 (front or back face). In the absence of crack opening, the brittle failure propagated axially from surface 1 to surface 7 (with $x_1 = 1.5875 \text{ mm}$) at an average speed of 945 m/s . We note that the crack speed in the two-dimensional (2-D) simulations was found to be 1.68 km/s [10]. Also, the opening of a crack due to brittle failure noticeably delayed the initiation of ductile failure.

We note that the CPU time required to solve the problem with DYNA3D is much less than that taken by our code. This is because of 3 degrees of freedom per

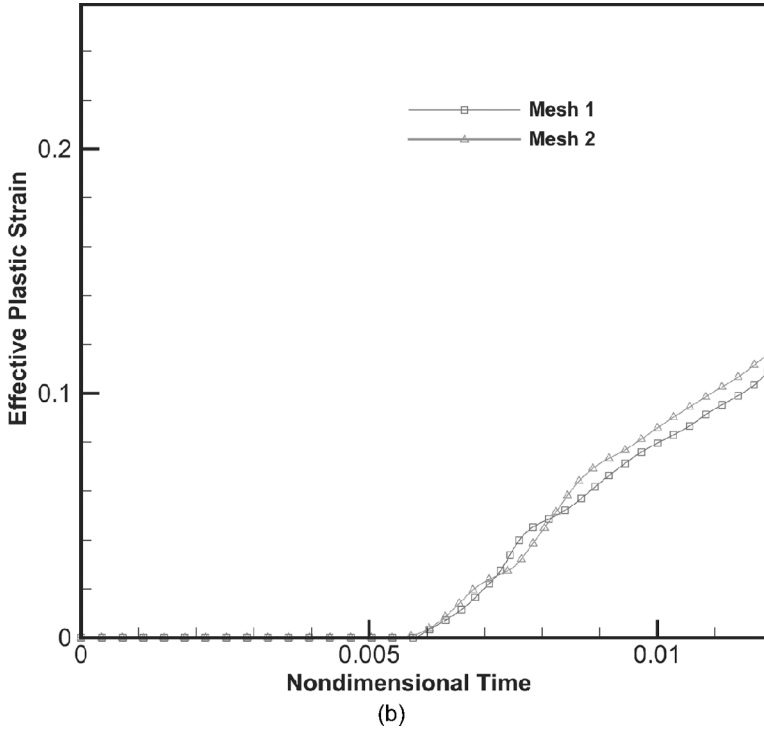
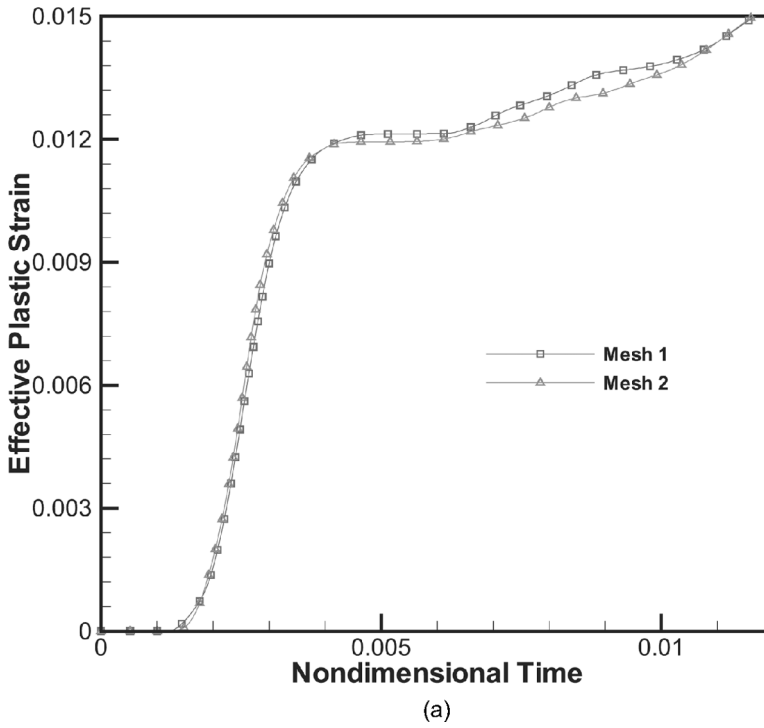


Figure 3 Time histories, computed with the two FE meshes, of the evolution of the effective plastic strain at one point (a) on the impacted face of the plate, and two points on the surface of the notch tip.

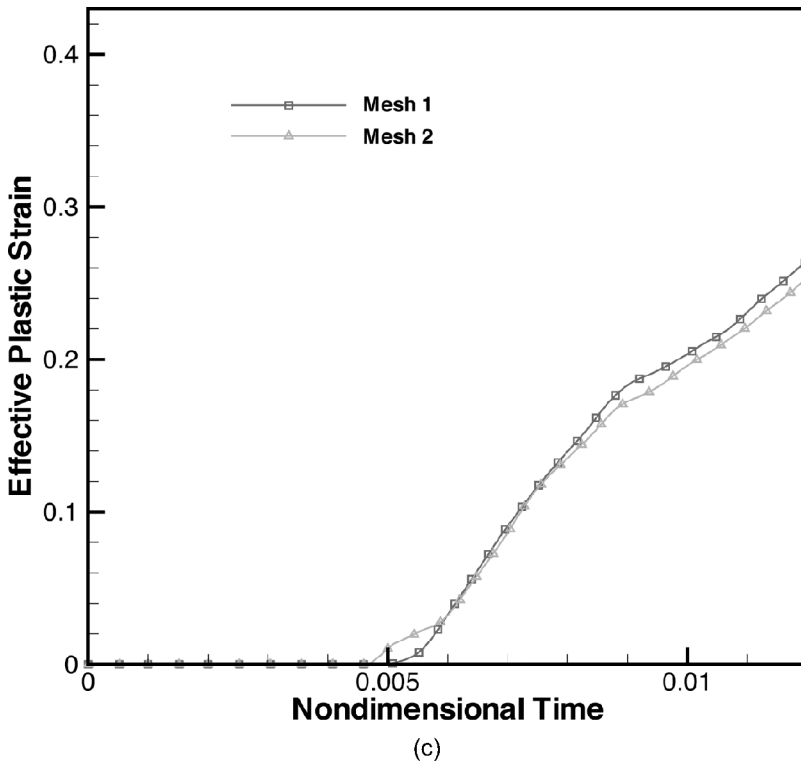


Figure 3 Continued.

node in DYNA3D and 15 in the present code, 1 integration point in DYNA3D and 8 in the present code, and the neglect of heat conduction in DYNA3D but not in the present code. However, artificial viscosity is used in DYNA3D to eliminate spurious modes but not in the present code. The time-step size in DYNA3D is proportional to the smallest time taken by a dilatational wave to propagate through an element but is adaptively adjusted in the present code in order to compute the solution within the prescribed accuracy. The consideration of heat conduction requires that the time step be smaller of those needed to compute a stable solution of the mechanical and the thermal problems. The time step drops significantly once an ASB has initiated.

Other differences between DYNA3D and our code are summarized next. DYNA3D neglects heat conduction, porosity evolution, and thermal stresses, and integrates constitutive relation (6) and the balance of internal energy at an integration point, i.e., the centroid of an element. Our code accounts for heat conduction, porosity evolution, and degradation of material parameters due to porosity, and also takes temperature, stresses, the porosity and the effective plastic strain at nodes as variables. Although the temperature and stresses are taken to be uniform within an element in DYNA3D they are assumed to vary in the present code.

Another code frequently used for the analysis of thermoviscoplastic problems is *ABAQUS* explicit. To the best of our knowledge, effects of heat conduction, thermal expansion, and porosity evolution are also neglected in this code.

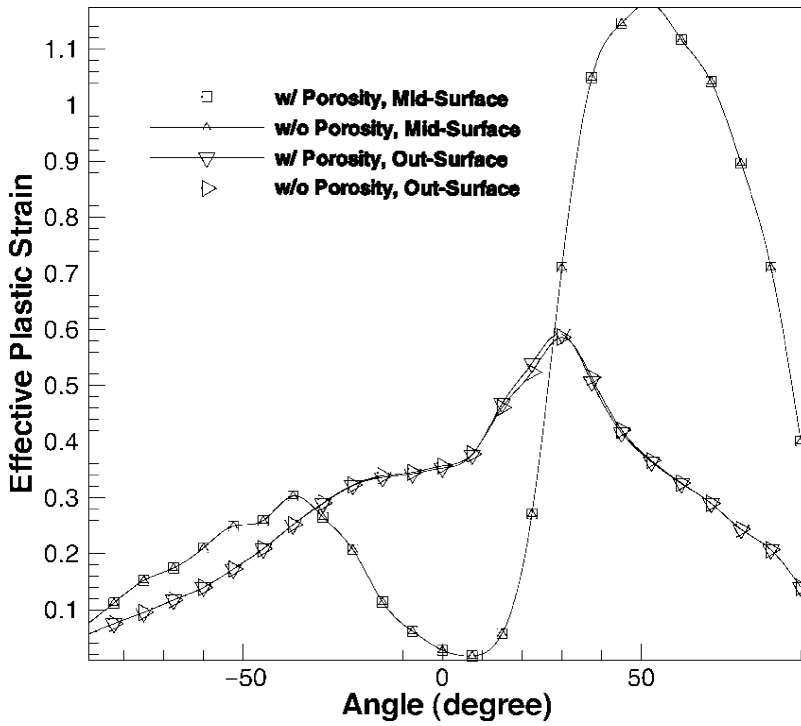


Figure 4 Variation of the effective plastic strain at points on the notch tip surface at time $t = 32 \mu\text{s}$.

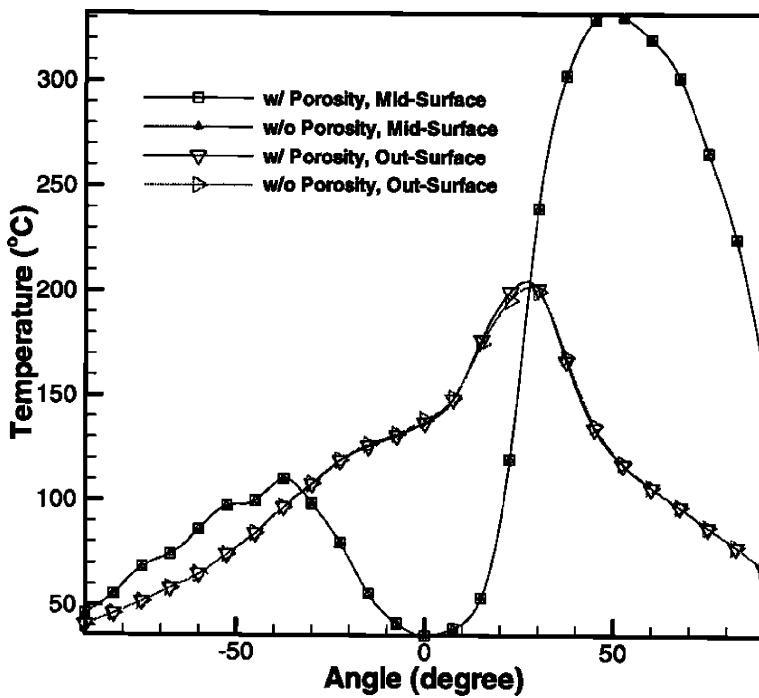


Figure 5 Variation of the temperature at points on the notch tip surface at time $t = 32 \mu\text{s}$.

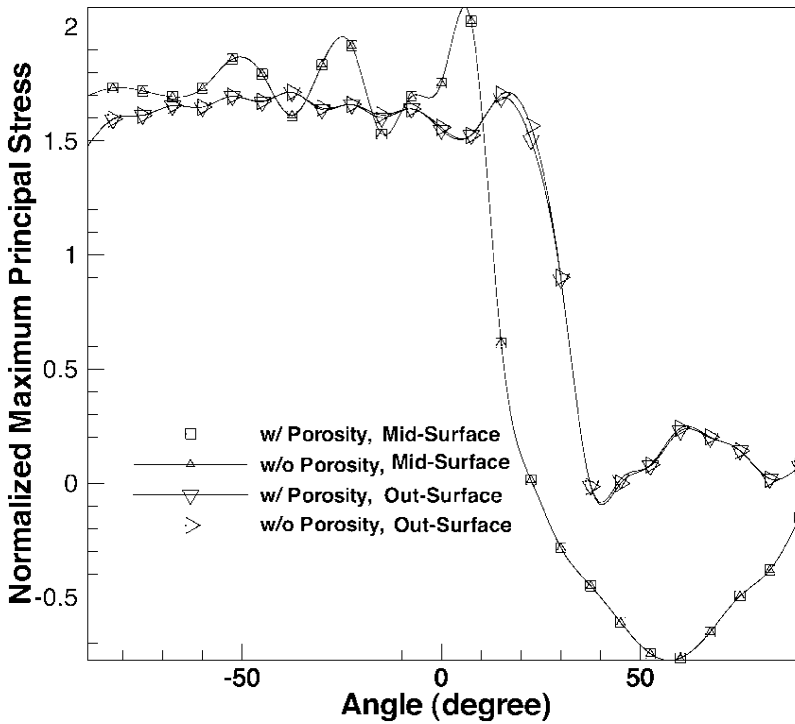


Figure 6 Variation of the maximum principal stress at points on the notch tip surface at time $t = 32 \mu\text{s}$.

Failure Criteria

Brittle failure is assumed to ensue at a material point when the maximum principal tensile stress there equals 2.34 times the quasistatic yield stress of the material. The initiation of ductile failure at a point is taken to be synonymous with the initiation of an ASB. Batra and Kim [23], based on their numerical experiments on simple shearing deformations of 12 materials, have proposed that an ASB initiates at a material point when the maximum shear stress there has dropped to 80% of the peak shear stress at that point and the material point is deforming plastically. For the 3-D problem studied here, we found it more convenient to use the following strain-based criterion. For the 4340 steel, an ASB is taken to initiate at a point when the effective plastic strain there reaches 0.6 and it is deforming plastically. This value was deduced from Batra and Ravisankar's [2] analysis of 3-D deformations of the prenotched 4340 steel plate.

Effect of FE Mesh

Results have been computed for two FE meshes that differ mainly in the region around the notch tip where severe deformations occur. The discretization into finite elements of the midsurface near the notch tip for one of these meshes is depicted in Figure 2. In mesh 1 the region near the notch tip is divided into finer elements than that in mesh 2. In each case, the half-thickness of the plate is divided into 10 layers

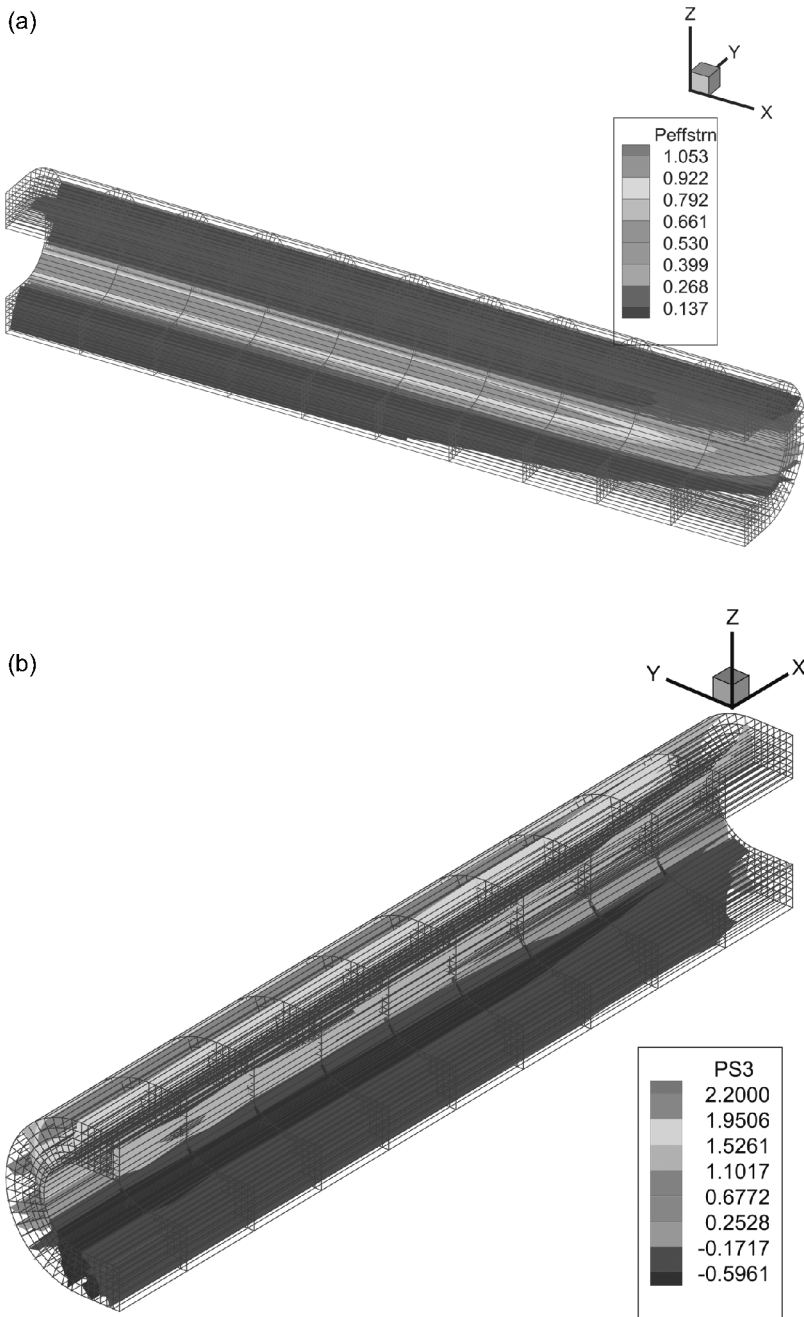


Figure 7 At time $t = 32 \mu\text{s}$, fringe plots in the reference configuration of (a) the effective plastic strain and (b) the maximum principal tensile stress at points on the notch tip surface.

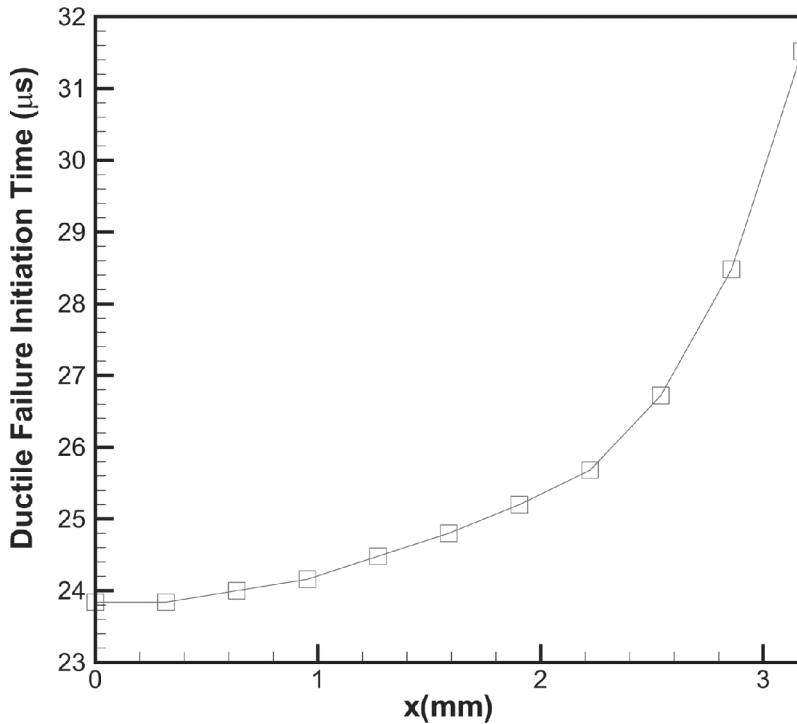


Figure 8 Variation of the ductile failure initiation time with the axial distance x from the plate's midsurface.

of equal thicknesses; meshes 1 and 2 have 39,952 and 31,251 nodes respectively. A finer mesh could not be used for a lack of computational resources. For the two FE meshes, time histories of the evolution of the effective plastic strain at three points, two of which are on the surface of the notch tip and the third one on the impacted face, are plotted in Figure 3a–c. It is clear that results computed with the two meshes are close to each other signifying very small dependence of computed results on the FE mesh employed. Results presented later have been computed with the FE mesh of 39,952 nodes.

One way to eliminate the effect of the FE mesh on computed results is to use a strain-rate gradient-dependent viscoplastic theory such as that employed in refs. [24]–[26]. It introduces material characteristic lengths that can not be easily estimated. Another possibility is to use adaptively refined FE meshes like those in refs. [27]–[29] for one- and two-dimensional problems, or a meshless method [30].

Table 1 Failure initiation times and locations

Failure mode	Location	Time of initiation (μs)
Ductile	Midsurface	23.84
	Front or back surface	31.48
Brittle	Midsurface	29.68
	Surface 1.588 mm away from the midsurface	31.36

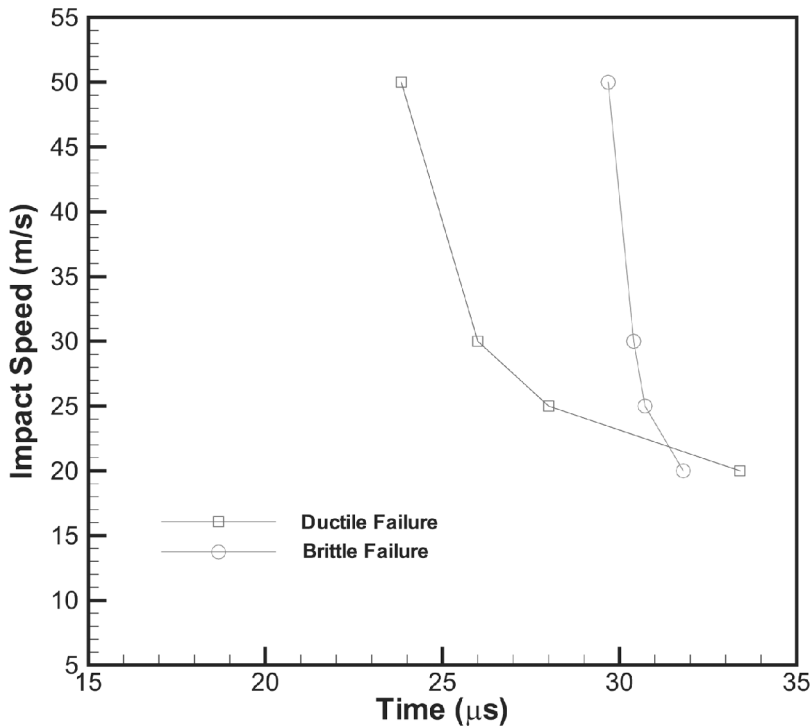


Figure 9 Variations with the impact speed of times of initiation of the brittle and the ductile failures.

Effect of Porosity Evolution

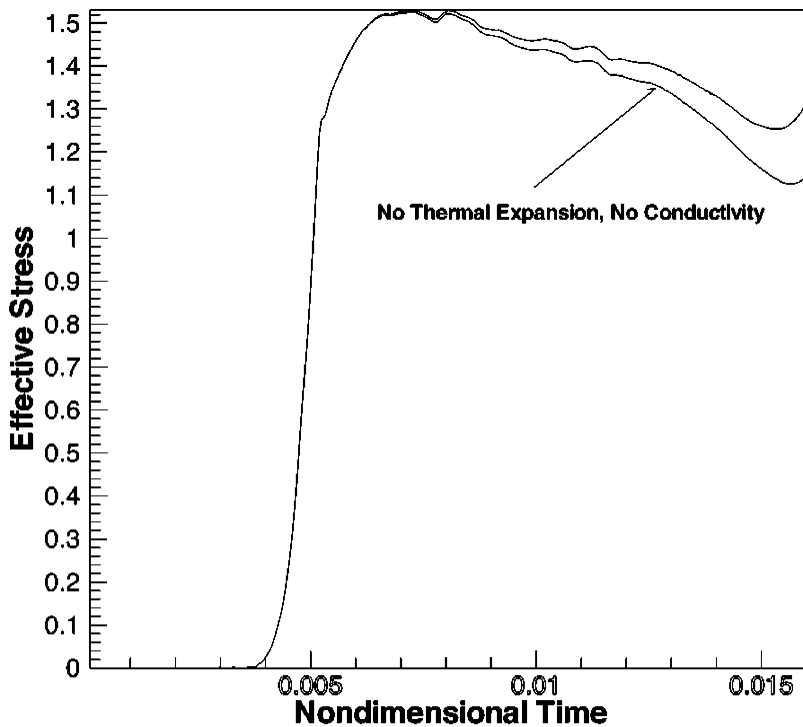
For an impact speed of 50 m/s, Figure 4 exhibits the variation of the effective plastic strain at points on the notch surface that are either on the midsurface or on the outermost (front or back) surfaces of the plate. Note that the positive angle is measured clockwise from the notch axis. Results were computed with and without the consideration of the porosity evolution. These plates show that the porosity has virtually no effect on the distribution of the effective plastic strain. This is mainly because not enough time has elapsed for the porosity to attain a value significant enough to soften the material. If the computations were performed for a longer time, then the porosity would have evolved significantly at points within an ASB (e.g., see [10]) and changed results at some locations. However, results could not be computed for longer times because of excessive distortion of one element adjoining the notch-tip surface. The angular variation of the effective plastic strain at points on the midsurface of the plate differs quantitatively and qualitatively from that at points on the outermost surfaces. Furthermore, the maximum value of the effective plastic strain reached at a point on the midsurface of the plate is nearly twice of that at a point on the outermost surfaces. Thus an ASB will initiate first at a point on the midsurface of the plate and lying on the notch tip. The angular variation of the temperature at points on the notch surface is very similar to that of the effective plastic strain; see Figure 5. The maximum

temperature rise at a point on the notch-tip that is on the midsurface of the plate equals 305 K but that of a point either on the front or on the back surface of the plate equals 175 K.

The angular distribution of the maximum principal stress at points on the notch surface is depicted in Figure 6. As for the effective plastic strain, the consideration of porosity evolution has virtually no effect on the values of the nondimensional maximum principal stress ($=\sigma_p/\sigma_0$). The qualitative distributions of the maximum principal stress on the midsurface and the front surface are similar. The magnitudes of the tensile stresses at similarly situated points on the midsurface and the front surface are not that much different. However, the maximum magnitude of the compressive principal stress at a point on the midsurface is considerably higher than that at a point on the front surface of the plate.

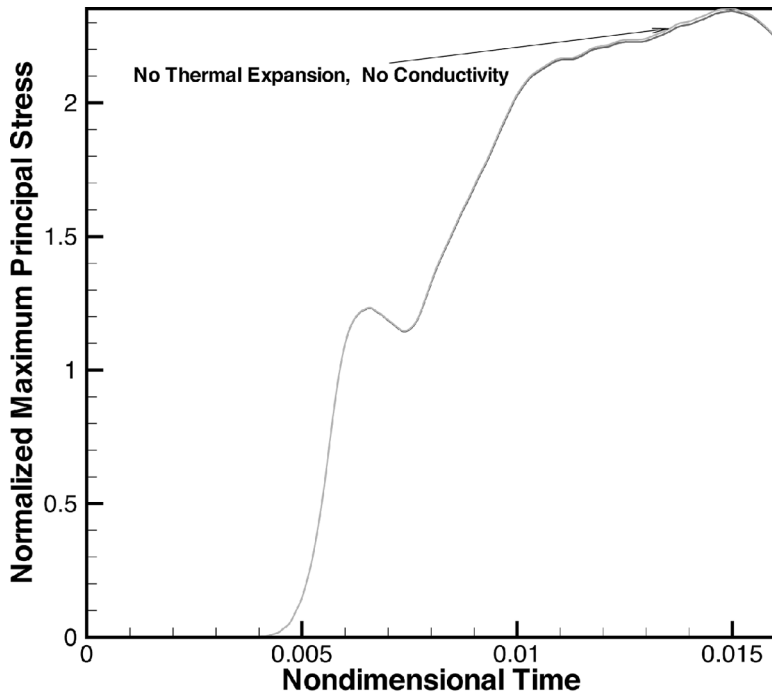
Failure-Mode Transition Speed

Results plotted in Figures 4 and 6 reveal that an ASB will first initiate at a point situated on the midsurface of the plate. The radial line passing through this

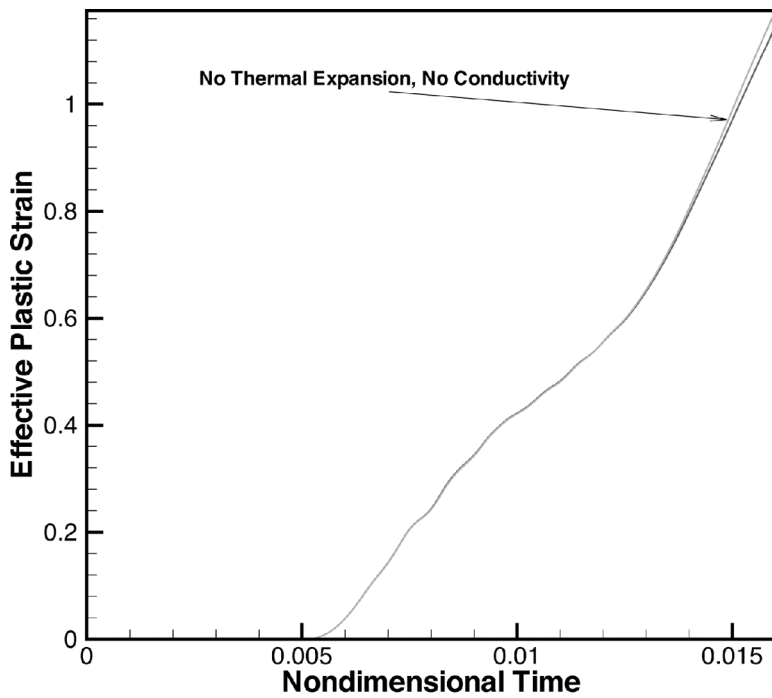


(a)

Figure 10 Time history of (a) the evolution of the effective stress, (b) the maximum principal tensile stress, and (c) the effective plastic strain at selected points with and without the effects of heat conduction and thermal expansion; the two curves in (b) and (c) essentially overlap each other.



(b)



(c)

Figure 10 Continued.

Table 2 Influence of thermal effects on failure initiation time (μs)

Thermal expansion and heat conduction	Ductile failure	Brittle failure
Yes	23.84	29.68
No	23.76	29.12

point makes an angle of about 50° clockwise from the notch axis. Brittle failure will ensue from a point on the upper surface of the notch tip and situated on the midsurface of the plate. Fringes of the effective plastic strain on the notch surface at time $t = 32 \mu\text{s}$ plotted in Figure 7a clearly show that the severely deformed region is concentrated near the midsurface of the plate and that the effective plastic strain gradually decreases as one moves toward an outermost surface of the plate. Fringe plots of the maximum principal tensile stress are depicted in Figure 7b. It is evident that the brittle failure has propagated only through half of the plate thickness. For an impact speed $V_0 = 50 \text{ m/s}$, Figure 8 evinces the variation of the failure initiation times as a function of the axial distance, x , from the midsurface of the

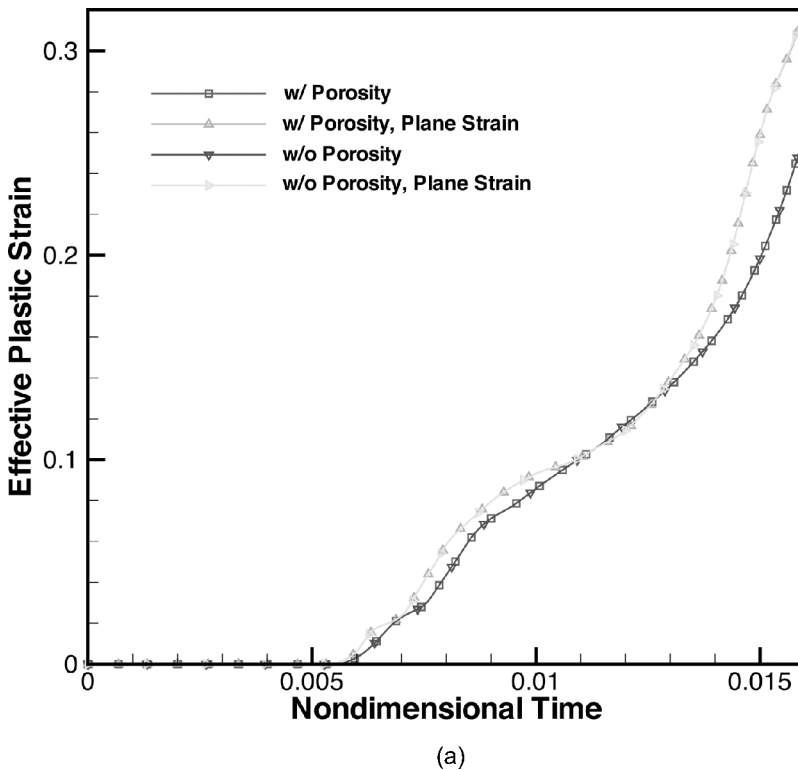
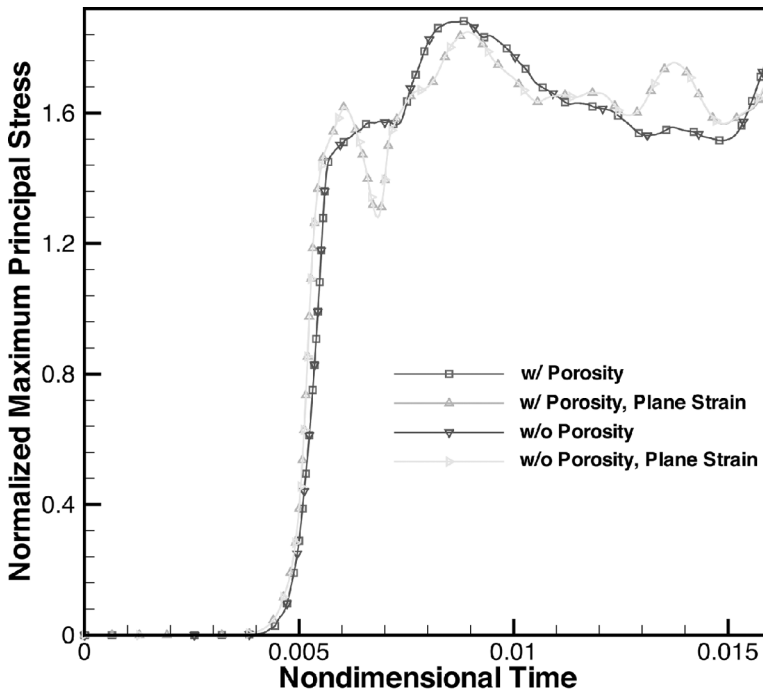
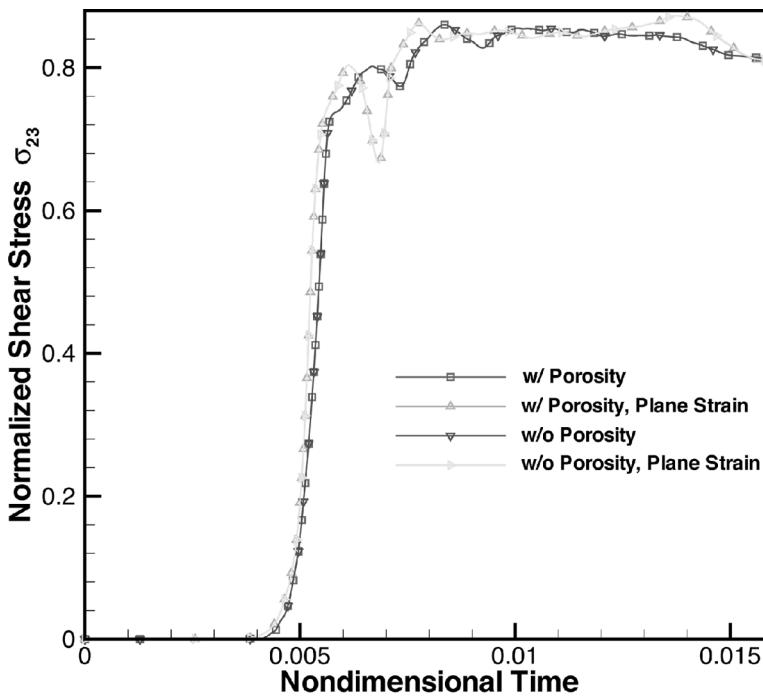


Figure 11 At node 540 with coordinates (0, 49.956 mm, 25.256 mm) in the reference configuration, time histories of (a) the effective plastic strain, (b) the normalized maximum principal stress, and (c) the normalized in-plane shear stress σ_{23} .



(b)



(c)

Figure 11 Continued.

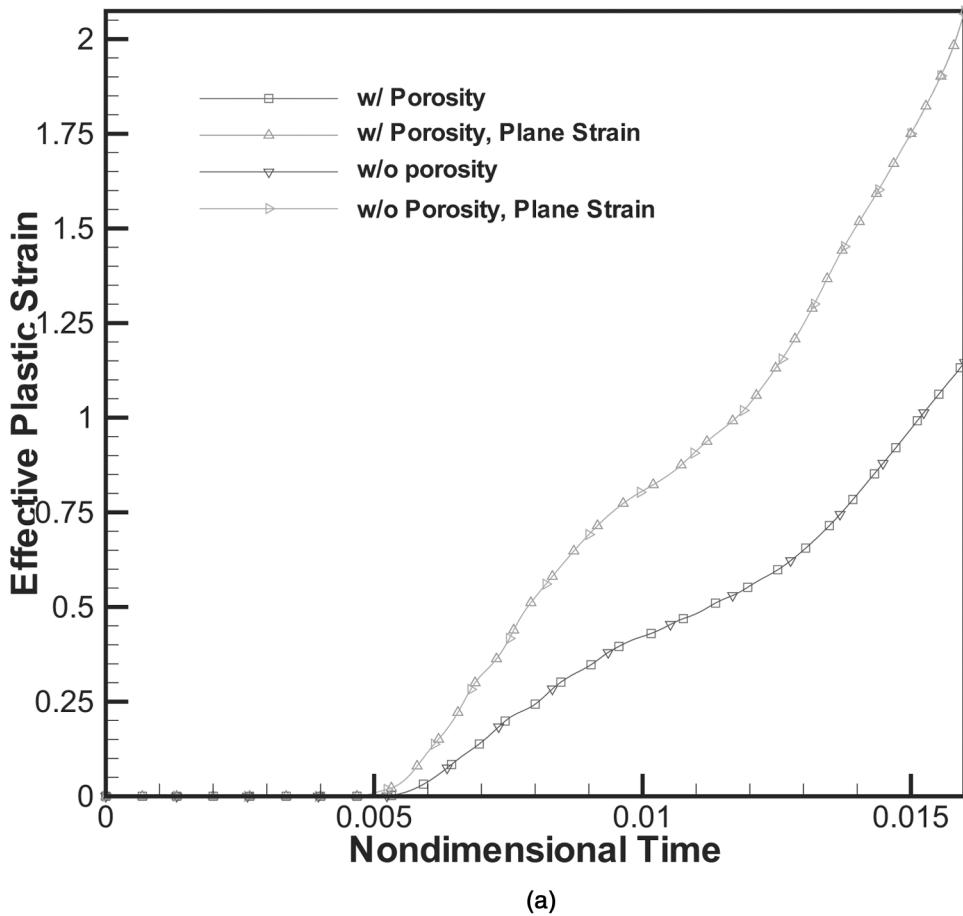
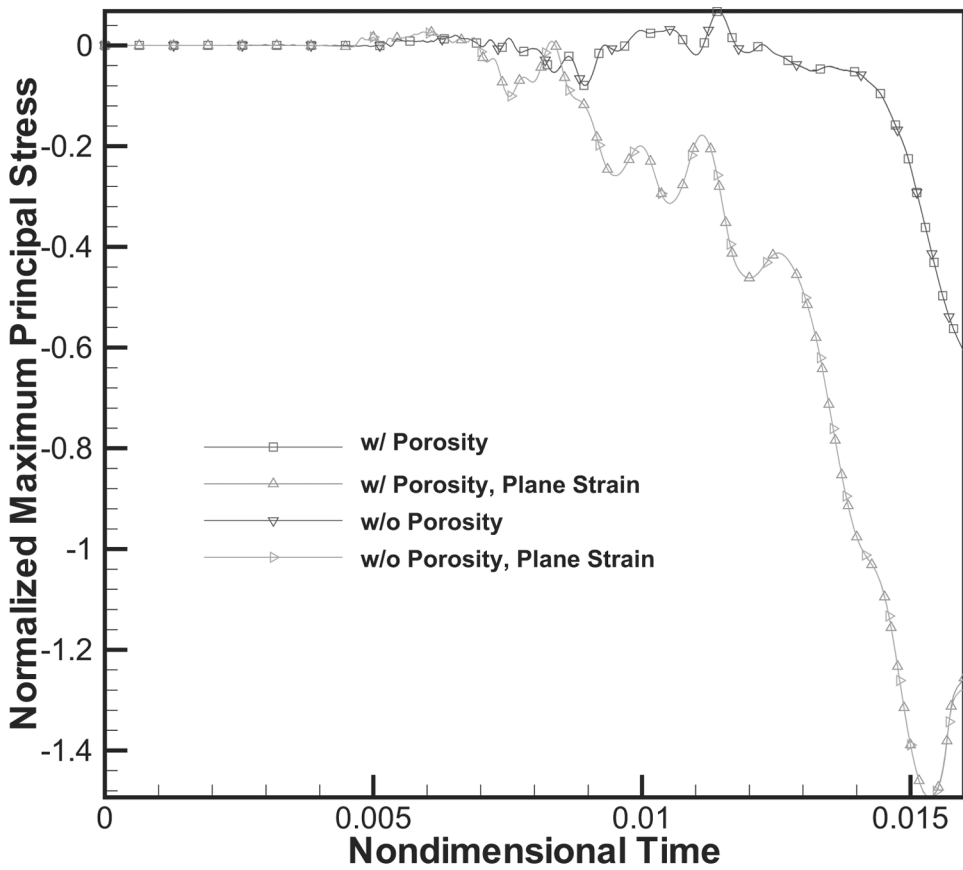


Figure 12 At node 1464 located at (0, 49.956 mm, 25.044 mm) in the reference configuration, time histories of (a) the effective plastic strain, (b) the normalized maximum principal stress, and (c) the normalized in-plane shear stress σ_{23} .

plate. The ductile failure at a point on the midsurface initiates at $t = 23.84 \mu\text{s}$, and at a point on the front or the back face of the plate ensues at $31.48 \mu\text{s}$, that is, $7.64 \mu\text{s}$ later than that at the midsurface. When the computations were stopped due to excessive distortions of an element, the brittle failure had propagated only through half of the plate thickness. Times of initiation of the brittle failure at the midsurface ($x = 0$) and on the notch surface with $x = 1.588 \text{ mm}$ equaled 29.68 and $31.36 \mu\text{s}$, respectively. Thus the average axial (in the thickness direction) velocities of propagation of the ductile and the brittle failures equal 413 m/s and 945 m/s , respectively. Note that no cracks are assumed to open at points where these failures initiate. Batra and Lear [10] have shown that, during plane strain deformations of the plate, the opening of a crack at the point where brittle failure initiates delays noticeably the onset of the ductile failure. The aforesaid results are summarized in Table 1.



(b)

Figure 12 Continued.

We have plotted in Figure 9 the dependence of the times of initiation of the brittle and the ductile failures upon the impact speed. These plots reveal that the brittle failure will initiate first for impact speeds below ~ 21.8 m/s and the ductile failure at impact speeds above ~ 21.8 m/s. The failure-mode transition speed depends upon the notch-tip radius, the material parameters, whether deformations are modeled as plane strain or 3-D, the failure criteria, whether or not cracks are allowed to open and propagate, and the viscoplastic relation.

Effect of Heat Conduction and Thermal Expansion

The effect of heat conduction and thermal expansion on the time history of the evolution of the effective stress, the effective plastic strain, and the maximum principal tensile stress at selected points is shown in Figure 10a–c. The plots of Figure 10a evince that the rate of drop of the effective stress is higher in the absence

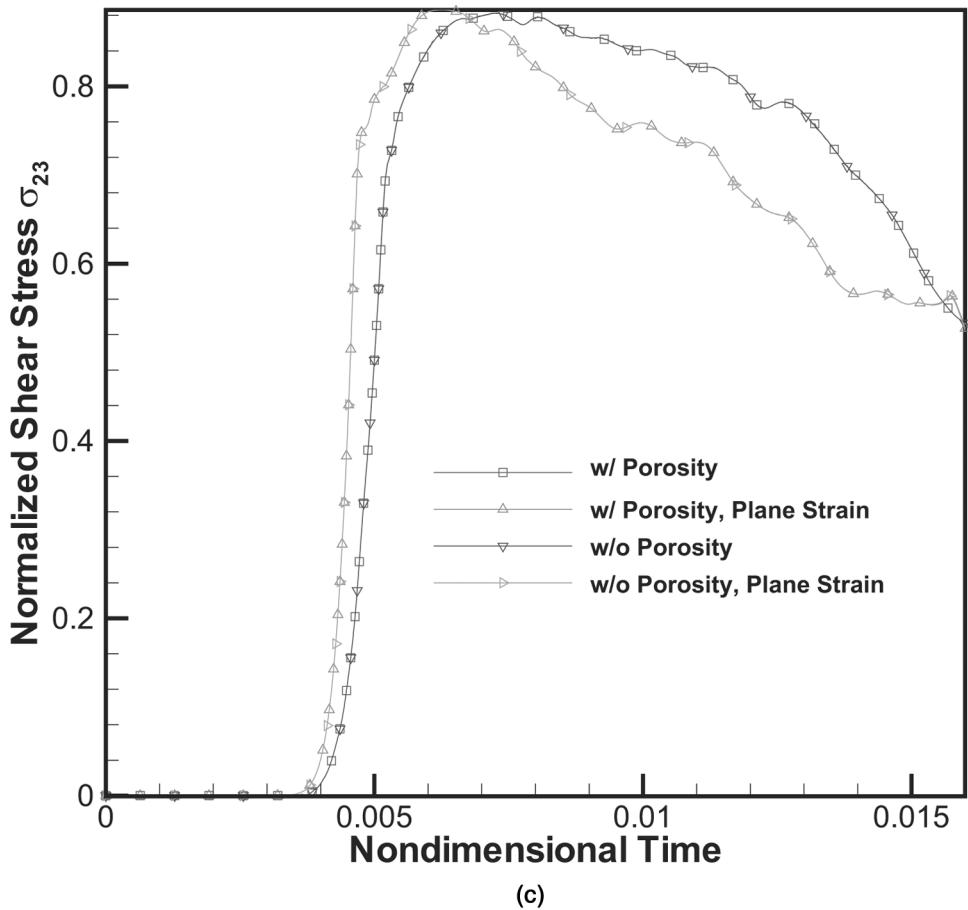


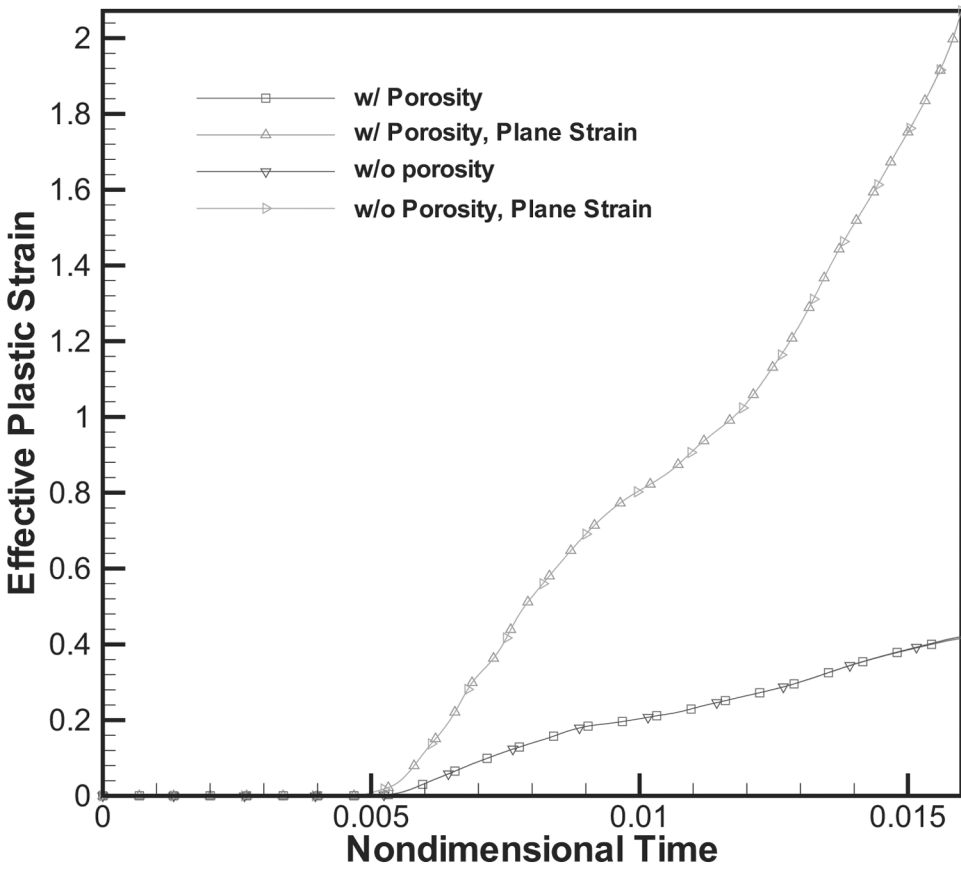
Figure 12 Continued.

of these two effects than that when they are considered. Thus the postlocalization response of the body is noticeably influenced by the consideration of thermal effects. Note that the two curves in Figures 10b and 10c overlap each other. The times of initiation of the two failure modes with and without the consideration of heat conduction and thermal expansion are summarized in Table 2.

Even though failure initiation times are virtually unaffected by the neglect of heat conduction and thermal expansion, the width of an ASB can only be computed when either heat conduction or strain gradients or both are considered. Otherwise, the ASB width is strongly influenced by the FE mesh employed and continues to decrease with successive refinements of the FE mesh.

Comparison of Results from 3-D and Plane Strain (2-D) Simulations

In order to compare results from the 2-D and the 3-D simulations we computed the 2-D solution by constraining in the thickness direction the motion of



(a)

Figure 13 At node 1884 located at (3.175 mm, 49.996 mm, 25.044 mm) in the reference configuration, time histories of (a) the effective plastic strain, (b) the normalized maximum principal stress, and (c) the normalized in-plane shear stress σ_{23} .

all nodes. We have plotted in Figures 11a–c the time histories of the evolution of the effective plastic strain, the normalized maximum principal stress and the normalized in-plane shear stress σ_{23} at node 540 with coordinates (0, 49.956 mm, 25.256 mm) in the reference configuration. Similar results at nodes 1464 and 1884 situated in the reference configuration at (0, 49.956 mm, 25.044 mm) and (3.175 mm, 49.996 mm, 25.044 mm) are depicted in Figures 12a–c and 13a–c, respectively. Nodes 540 and 1464 are on the midsurface of the plate and node 1884 is on an outermost face. At node 540, the two time histories of evolution of each of the three quantities computed from the 2-D and the 3-D simulations essentially agree with each other for $0 \leq t \leq 0.013$ (or $26 \mu\text{s}$). For $t > 0.013$, the 2-D analysis gives higher value of the effective plastic strain than the 3-D analysis. This difference between the two values of the effective plastic strain continues to increase with time. At nodes 1464 and 1884, there are significant differences

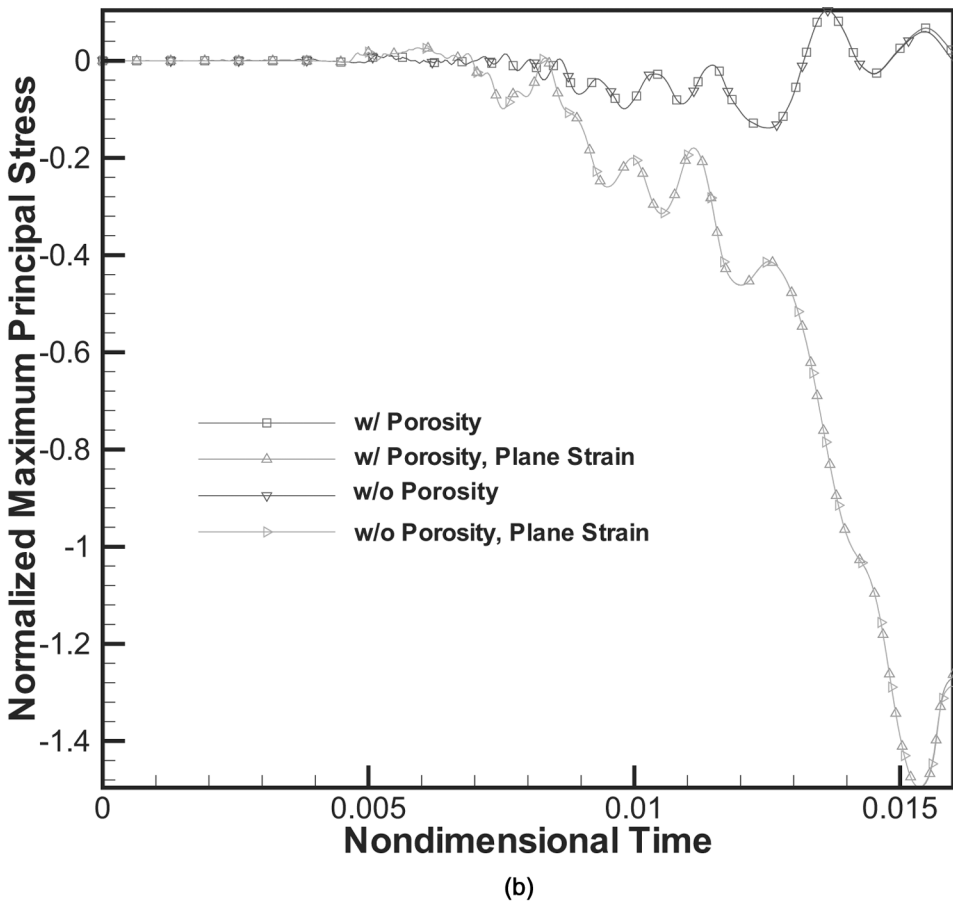


Figure 13 Continued.

in the two sets of values of each one of the three quantities. The failure initiation times from the 2-D and the 3-D analyses are summarized in Table 3. It is clear that the two analyses predict significantly different times of initiation of the ductile failure. The initiation times for the brittle and the ductile failures from the 2-D analysis are about 10% and 36% less than those from the 3-D analysis. Like the time history of evolution of the effective plastic strain, time histories of evolution of the maximum (in magnitude) principal stress and the in-plane shear stress at nodes 1464 and 1884 computed from the 2-D and the 3-D analyses differ noticeably.

Because of significant differences in the times of initiation of failures in the 2-D and the 3-D analyses, the failure mode transition speed predicted from these two analyses will also be quite different. Thus, unless the 2-D and the 3-D analyses give very close results, the validity of a constitutive relation can only be established by comparing experimental observations with results computed from the 3-D analysis.

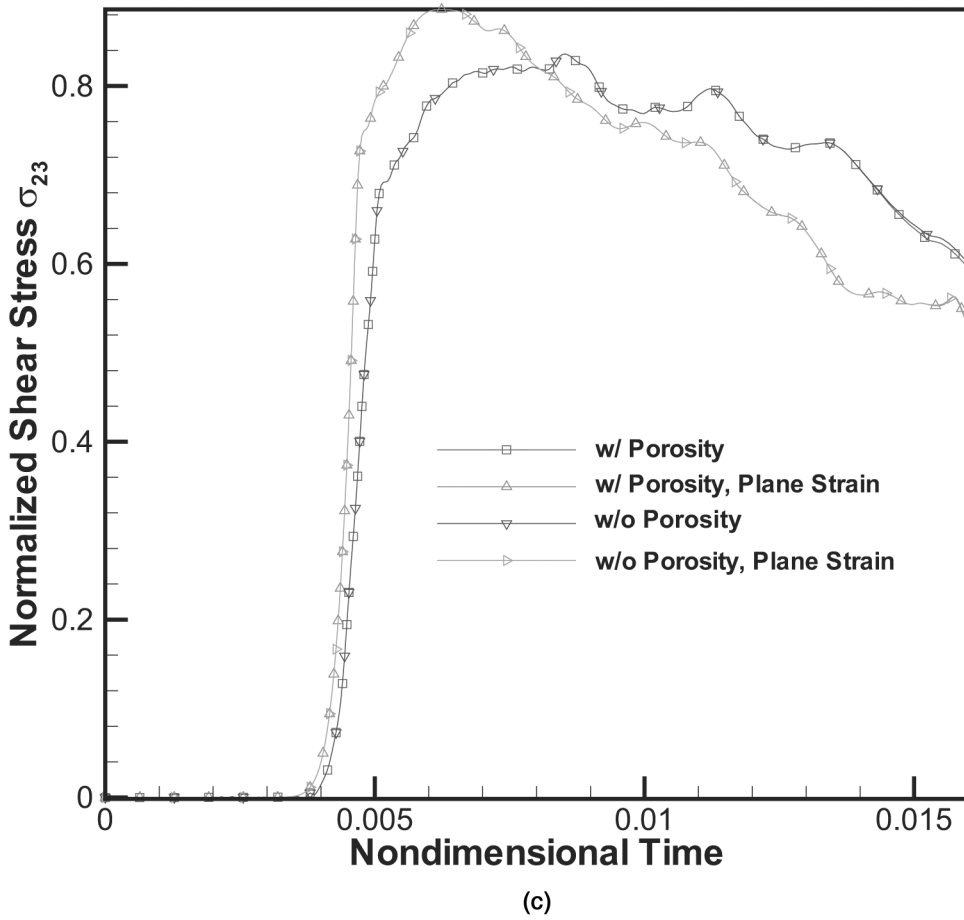


Figure 13 Continued.

Viscoplastic Relation

As stated in the introduction, different viscoplastic relations calibrated to the same test data for simple shear deformations give qualitatively similar but quantitatively quite different results for ASB initiation times, the postlocalization response, and the spacing between adjacent shear bands; for example; see refs [7], [11], and [31].

Table 3 Failure initiation time (μs) from the 3-D and the 2-D analyses

Analysis	Ductile	Brittle
3-D	23.84	29.68
2-D	15.20	27.12

CONCLUSIONS

We have analyzed, by the finite-element method, three-dimensional (3-D) transient thermomechanical deformations of a heat-conducting isotropic, homogeneous, microporous, and thermoviscoplastic prenotched plate. We have developed a computer code that employs a Lagrangian mesh but adjusts the time step adaptively in order to compute the solution within the prescribed accuracy. The problem formulation includes the degradation of material properties due to porosity. It is found that both the brittle and the ductile failures initiate at points either on or close to the notch-tip surface and lying on the midsurface of the plate. With crack opening not modeled, the ductile failure in the form of an adiabatic shear band propagates in the thickness direction with speed varying from 1984 m/s from the point of initiation on the plate's midsurface to 104 m/s when it arrives at the front or the back face of the plate. An experimentalist making observations on the outermost surfaces of the plate will see ductile failure initiate at $t = 31.48 \mu\text{s}$, but it occurred on the midsurface at $23.84 \mu\text{s}$. For the material parameters used in this study the failure mode transitions from brittle to ductile at an impact speed of 21.8 m/s.

A comparison of results from the 3-D and the 2-D (plane strain) analyses of the same problem reveals that an adiabatic shear band initiates much sooner in the 2-D simulations than in the 3-D simulations. For the problem studied, these times are $15.2 \mu\text{s}$ and $23.84 \mu\text{s}$ for the 2-D and the 3-D analyses, respectively. The 2-D and the 3-D analyses will give noticeably different failure mode transition speeds. Because of significant differences in results from the 2-D and the 3-D analyses, it is recommended that the validity of a constitutive relation be established by comparing test findings with results of 3-D analyses.

REFERENCES

1. J. F. Kalthoff, Modes of Dynamic Shear Failure in Solids, *Int. J. Fracture*, vol. 101, pp. 1–31, 2000.
2. R. C. Batra and M. V. S. Ravisankar, Three-dimensional Numerical Simulation of the Kalthoff Experiment, *Int. J. Fracture*, vol. 105, pp. 161–186, 2000.
3. R. C. Batra and N. V. Nechitailo, Analysis of Failure Modes in Impulsively Loaded Prenotched Plates, *Int. J. Plasticity*, vol. 13, pp. 291–308, 1997.
4. R. C. Batra and R. R. Gummalla, Effect of Material and Geometric Parameters on Deformations near the Notch Tip of a Dynamically Loaded Prenotched Plate, *Int. J. Fracture*, vol. 101, pp. 99–140, 2000.
5. A. Needleman and V. Tvergaard, Analysis of Brittle–Ductile Transition under Dynamic Shear Loading, *Int. J. Solids Struct.*, vol. 32, pp. 2571–2590, 1995.
6. M. Zhou, G. Ravichandran, and A. J. Rosakis, Dynamically Propagating Shear Bands in Prenotched Plates: II—Finite Element Simulations, *J. Mech. Phys. Solids*, vol. 44, pp. 1007–1032, 1996.
7. R. C. Batra and N. A. Jaber, Failure Mode Transition Speeds in an Impact Loaded Prenotched Plate with Four Thermoviscoplastic Relations, *Int. J. Fracture*, vol. 110, pp. 47–71, 2001.
8. R. C. Batra and N. A. Jaber, Effect of Specimen Height on the Initiation of Failure in an Impact Loaded Prenotched Plate, In: *Plasticity, Damage and Fracture at Macro, Micro and Nano Scales* (ed. A. S. Khan and O. Lopez-Pamies), Neat Press, Fulton, pp. 633–635, 2002.

9. R. C. Batra, N. A. Jaber, and M. E. Malsbury, Analysis of failure modes in an impact loaded thermoviscoplastic prenotched plate, *Int. J. Plasticity*, vol. 19, pp. 139–196, 2003.
10. R. C. Batra and M. H. Lear, Simulation of Brittle and Ductile Fracture in an Impact Loaded Prenotched Plate, *Int. J. Fracture*, vol. 126, pp. 179–203, 2004.
11. R. C. Batra and C. H. Kim, Effect of Viscoplastic Flow Rules on the Initiation and Growth of Shear Bands at High Strain Rates, *J. Mech. Phys. Solids*, vol. 38, pp. 859–874, 1990.
12. M. Zhou, G. Ravichandran, and A. Rosakis, Dynamically Propagating Shear Bands in Impact-Loaded Prenotched Plates, I, *J. Mech. Phys. Solids*, vol. 44, pp. 981–1006, 1996.
13. J. J. Mason, A. J. Rosakis, and G. Ravichandran, Full Field Measurements of the Dynamic Deformation Field Around a Growing Adiabatic Shear Band at the Tip of a Dynamically Loaded Crack or a Notch, *J. Mech. Phys. Solids*, vol. 42, pp. 1679–1697, 1994.
14. K. Ravi-Chandar, J. Lu, B. Yang, and Z. Zhu, Failure Mode Transitions in Polymers Under High Strain Rate Loading, *Int. J. Fracture*, vol. 101, pp. 33–72, 2000.
15. A. L. Gurson, Continuum Theory of Ductile Rupture by Void Nucleation and Growth: Part I, *J. Eng. Mater. Tech.*, vol. 99, pp. 2–15, 1977.
16. V. Tvergaard, Influence of Voids on Shear Band Instabilities Under Plane Strain Conditions, *Int. J. Fracture*, vol. 17, pp. 389–407, 1981.
17. G. R. Johnson and W. H. Cook, A Constitutive Model and Data for Metals Subjected to Large Strains, High Strain-Rates, and High Temperatures, *Proc. 7th Int. Symp. on Ballistics*, 1983.
18. C. Chu and A. Needleman, Void Nucleation Effects in Biaxially Stretched Sheets, *J. Eng. Mater. Tech.*, vol. 102, pp. 249–256, 1980.
19. V. Tvergaard and A. Needleman, Analysis of the Cup-Cone Fracture in a Round Tensile Bar, *Acta Metall.*, vol. 32, pp. 157–169, 1984.
20. P. Perzyna, Constitutive Modeling of Dissipative Solids for Localization and Fracture, In: *Localization and Fracture Phenomenon in Inelastic Solids*, (ed. P. Perzyna), pp. 99–242, Springer, Berlin, 1998.
21. R. C. Batra and X. S. Jin, Analysis of Dynamic Shear Bands in Porous Thermally Softening Viscoplastic Materials, *Arch. Mech.*, vol. 41, pp. 354–369, 1994.
22. T. J. R. Hughes, *The Finite Element Method*, Prentice Hall, Englewood Cliffs, NJ, 1987.
23. R. C. Batra and C. H. Kim, Analysis of Shear Bands in Twelve Materials, *Int. J. Plasticity*, vol. 8, pp. 425–452, 1992.
24. R. C. Batra, The Initiation and Growth of, and the Interaction Among Adiabatic Shear Bands in Simple and Dipolar Materials, *Int. J. Plasticity*, vol. 3, pp. 75–89, 1987.
25. R. C. Batra and C. H. Kim, Adiabatic Shear Banding in Elastic-Viscoplastic Nonpolar and Dipolar Materials, *Int. J. Plasticity*, vol. 6, pp. 127–141, 1990.
26. R. C. Batra and J. Hwang, Dynamic Shear Band Development in Dipolar Thermoviscoplastic Materials, *Comput. Mech.*, vol. 12, pp. 354–369, 1994.
27. R. C. Batra and C. H. Kim, An Adaptive Mesh Refinement Technique for the Analysis of Adiabatic Shear Banding, *Mech. Res. Commun.*, vol. 17, pp. 81–91, 1990.
28. R. C. Batra and K. I. Ko, An Adaptive Mesh Refinement Technique for the Analysis of Shear Bands in Plane Strain Compression of a Thermoviscoplastic Solid, *Comput. Mech.*, vol. 10, pp. 369–379, 1992.
29. R. C. Batra and J. Hwang, An Adaptive Mesh Refinement Technique for Two-Dimensional Shear Band Problems, *Comput. Mech. Int. J.*, vol. 12, pp. 255–268, 1993.

30. R. C. Batra, G. M. Zhang, Analysis of Adiabatic Shear Bands in Elasto-Thermo-Viscoplastic Materials by Modified Smoothed-Particle Hydrodynamics (MSPH) Method, *J. of Computational Physics*, vol. 201, pp. 172–190, 2004.
31. R. C. Batra and L. Chen, Effect of Viscoplastic Relations on the Instability Strain, Shear Band Initiation Strain, the Strain Corresponding to the Minimum Shear Band Spacing, and the Band Width in a Thermoviscoplastic Materials, *Int. J. Plasticity*, vol. 17, pp. 1465–1489, 2001.